

Effect of the Molecular Structure on the Hierarchical Self-Assembly of Semifluorinated Alkanes at the Air/Water Interface

Laurence de Viguerie,[†] Rabea Keller,[‡] Ulrich Jonas,^{*,†} Rüdiger Berger,[‡] Christopher G. Clark, Jr.,[‡] Christopher O. Klein,[†] Thomas Geue,[§] Klaus Müllen,[‡] Hans-Jürgen Butt,[‡] and Dimitris Vlassopoulos^{†,||}

[†]Bio-Organic Materials Chemistry Laboratory, Institute of Electronic Structure & Laser, Foundation for Research and Technology—Hellas (FORTH), P.O. Box 1527, 71110 Heraklion, Greece

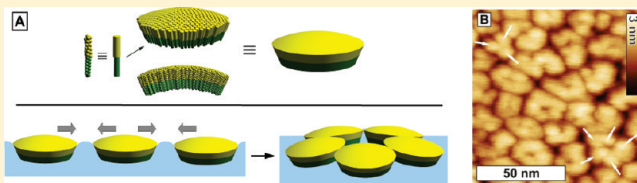
[‡]Max Planck Institute for Polymer Research, 55128 Mainz, Germany

[§]Laboratory for Neutron Scattering, Paul Scherrer Institut, 5232 Villigen, Switzerland

^{||}Department of Materials Science and Technology, University of Crete, Heraklion, Greece

S Supporting Information

ABSTRACT: Semifluorinated alkanes ($C_nF_{2n+1}C_mH_{2m+1}$), short F_nH_m display local phase separation of mutually incompatible hydrocarbon and fluorocarbon chain moieties, which has been utilized as a structure-forming motif in supramolecular architectures. The packing of semifluorinated alkanes, nominally based on dodecyl subunits, such as perfluoro-(dodecyl)dodecane ($F_{12}H_{12}$) and perfluoro-(dodecyl)eicosane ($F_{12}H_{20}$), as well as a core extended analogue, 1,4-dibromo-2-((perfluoroundecyl)methoxy)-5-(dodecyloxy)benzene ($F_{11}H_{11}$ -core- H_{12}), was studied at the air/water interface. Langmuir monolayers were investigated by means of neutron reflectivity directly at the air/water interface and scanning force microscopy after transfer to silicon wafers. Narrowly disperse surface micelles formed in all three cases; however, they were found to bear different morphologies with respect to molecular orientation and assembly dimensionality, which gives rise to different hierarchical aggregate topologies. For $F_{12}H_{12}$, micelles of ca. 30 nm in diameter, composed of several circular or “spherical cap” substructures, were observed and a monolayer model with the fluorocarbon block oriented toward air is proposed. $F_{12}H_{20}$ molecules formed larger (ca. 50 nm diameter) hexagonally shaped surface micelles that were hexagonally, densely packed, besides more elongated but tightly interlocked wormlike structures. Conversely, $F_{11}H_{11}$ -core- H_{12} films organized into linear rows of elongated surface micelles with comparable width, but an average length of ca. 400 nm, apparently formed by antiparallel molecular packing.



1. INTRODUCTION

Semifluorinated alkanes (SFAs, $C_nF_{2n+1}C_mH_{2m+1}$, F_nH_m) are known to form stable Langmuir monolayers at the air/water interface despite the hydrophobicity of both the alkyl chain and the fluorinated moiety.^{1,2} They have been widely studied in the literature because of their unique properties, determined by the strong incompatibility of fluorocarbon and hydrocarbon blocks, which drives molecular phase separation. In this respect, these so-called amphiphobic molecules can be considered as molecular analogues of incompatible diblock copolymers. In the bulk, they exhibit a richness of solid state packing structures. Moreover, they are applied for molecular interfacial film stabilization to improve colloidal systems of biological interest, such as liposomes employed as drug carriers, or in the fluorocarbon-in-water emulsions used as blood substitutes.^{3,4}

Significant efforts have been devoted to the investigation of their structures at the air/water interface, and different structural models have been proposed for various molecular architectures. While the molecular orientation and packing of an SFA carrying a hydrophilic head group at one end of the chain in contact with the water phase is rather straightforward and could be elucidated

to great detail at the air/water interface, e.g., by grazing-incidence X-ray diffraction,^{5–8} the situation is more ambiguous for the amphiphobic SFA structures without hydrophilic head groups. Examination of diverse F_nH_m diblocks indicated that they tend to self-assemble spontaneously at different characteristic length scales into “surface micelles” (circular or elongated).^{5,6} This aggregation behavior suggests that these molecules can be exploited as motifs for hierarchical organization. A major question in this context is the orientation of the molecules at the air/water interface. Different models of film structures, where molecules are oriented either parallel to each other or in a head-to-tail configuration, have been suggested on the basis of scanning force microscopy (SFM), X-ray reflectivity, and grazing-incidence small-angle X-ray scattering (GISAXS) measurements.^{9–11}

One of the investigated molecules, $F_{12}H_{12}$ (see Figure 1) has been previously studied for its propensity to form phase-separated, lamellar structures in the solid bulk state.^{12–16} More recent

Received: April 15, 2011

Revised: May 19, 2011

Published: June 14, 2011

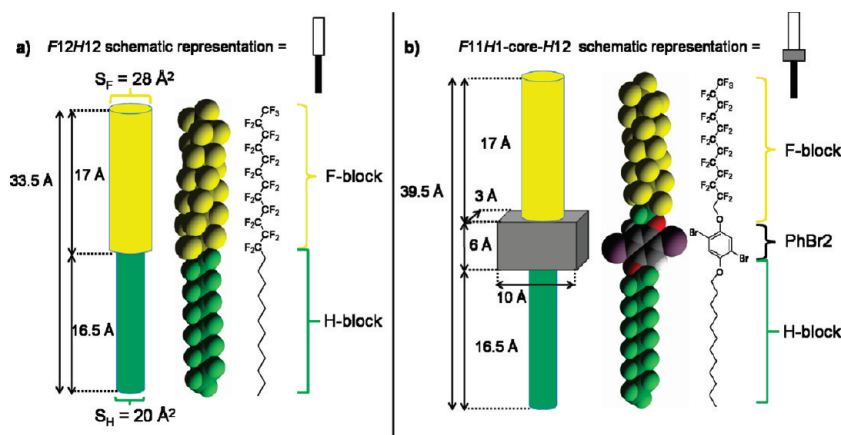
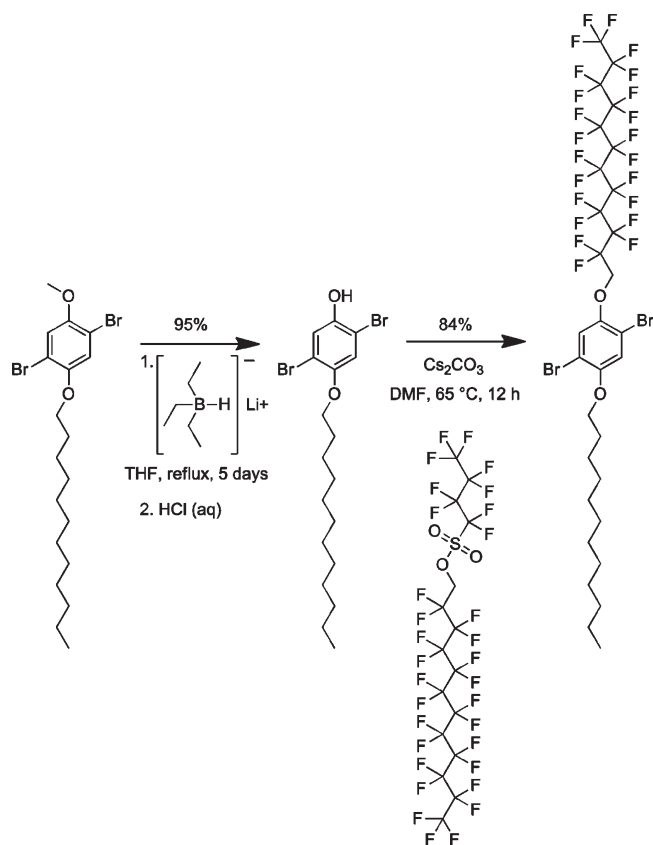


Figure 1. Chemical structures, molecular CPK models, and schematic representations of (a) *F12H12* (with *F12H20* being analogous, but with longer H-alkyl chain) and (b) *F11H1-core-H12*.

Scheme 1. Synthetic Route to *F11H1-core-H12* (1,4-Bibromo-2-((perfluoroundecyl)methoxy)-5-(dodecyloxy)benzene)



investigations using different complementary techniques (Brillouin light scattering spectroscopy, shear rheometry, X-ray scattering, solid state NMR, PVT measurements, etc.) have elaborated on the mechanism of the lamellar first-order phase transitions in three dimensions.^{17–19}

Herein, we report the aqueous surface-mediated self-assembly into molecularly thin films of SFAs *F12H12*, *F12H20*, and *F11H1-core-H12* (with a central 2,5-dibromo-1,4-phenyl core being connected to each of the two chains via ether linkages), and their structure investigation by scanning force microscopy to image the

monolayer morphology and neutron reflectivity to assess the molecular orientation within the layer and determine the layer thickness. To our knowledge, this is the first study to focus on the structural properties (besides previously reported isotherm data) of monolayers of semifluorinated alkane molecules with symmetric F- and H-block lengths. As these SFA-type molecules are attractive for novel organization motifs in two dimensions, it is of general interest whether similar block lengths induce specific self-assembly properties different from the reported asymmetric cases. Moreover, the results on the purely alkyl-based SFAs are contrasted with those of the core-extended molecule, which combines aromatic with alkyl moieties and is expected to feature different modes of intermolecular interactions.

2. EXPERIMENTAL SECTION

¹H, ¹³C, and ¹⁹F solution state NMR spectra were recorded on a Bruker AMX500 NMR spectrometer using the residual proton of the solvent (6.00 ppm for C₂H₂DCl₄) or the carbon signal of the deuterated solvent (73.78 ppm for C₂D₂Cl₄) as an internal standard. ¹⁹F NMR data were externally referenced using hexafluorobenzene in C₂D₂Cl₄ (−160.89 ppm). Field desorption mass spectra (FDMS) were performed with a VG-Instruments ZAB 2-SE-FDP using 8 kV accelerating voltage. Elemental analyses were performed by the Microanalytical Laboratory of Johannes Gutenberg University.

2.1. Materials. Cesium carbonate was dried in vacuo overnight at 100 °C. All other materials were used as received from Aldrich. Perfluoro(dodecyl)dodecane (*F12H12*) and perfluoro(dodecyl)eicosane (*F12H20*) were synthesized as previously reported.¹⁴ 1,4-Dibromo-2-((perfluoroundecyl)methoxy)-5-(dodecyloxy)benzene (*F11H1-core-H12*) was synthesized, as outlined in Scheme 1, by alkylation of 2,5-dibromo-4-dodecyloxyphenol²⁰ with 1-perfluoroundecylmethoxyborane²¹ in DMF using cesium carbonate as base. A methylene group adjacent to the aryl ether was employed instead of a CF₂ group, e.g., *F11H1* vs *F12*, so that the classical nucleophilic substitution could be carried out. The consequence is a slightly more flexible ether linkage, but essentially preserving the same overall helical conformations (left and right handed) as the SFA fluorocarbon moiety. The synthesis of 1,4-dibromo-2-dodecyloxy-5-methoxybenzene is described elsewhere.²⁰

2.1.1. 2,5-Dibromo-4-dodecyloxyphenol. A one-neck round-bottom flask, equipped with a reflux condenser, was charged with 1,4-dibromo-2-dodecyloxy-5-methoxybenzene (4.675 g, 10.38 mmol) and a solution of lithium triethyl borohydride or Super-Hydride (1.0 M in THF,

17.0 mL, 17.0 mmol). The reaction mixture was heated to reflux for 5 days under argon, cooled to 0 °C, and diluted with diethyl ether (200 mL), and the resulting mixture was quenched with water. The ether layer was washed with hydrochloric acid (aqueous, 5%) and brine. The organic phase was dried over MgSO₄, filtered, and concentrated in vacuo to yield a colorless oil (4.30 g, 95%). The product was identified by ¹H NMR, identical to that of previously reported alternative syntheses,^{22,23} and was used without further purification.

2.1.2. 1,4-Dibromo-2-((perfluoroundecyl)methoxy)-5-(dodecyloxy) benzene. A mixture of 2,5-dibromo-4-dodecyloxyphenol (2.0 g, 4.58 mmol) and 1-perfluoroundecylmethylnonaflate (4.45 g, 5.04 mmol) in DMF (45.8 mL) was degassed by bubbling with argon for 40 min. Cesium carbonate (2.25 g, 6.90 mmol) was added, and the reaction mixture was heated to 65 °C for 12 h. The reaction mixture was concentrated in vacuo and dissolved in refluxing ethyl acetate in water. The aqueous layer was extracted a second time with refluxing ethyl acetate. The organic layers were combined and washed with water, aqueous sodium hydroxide (5%), and brine. The organic mixture was dried over MgSO₄, adsorbed to silica gel (9 g) in vacuo, and chromatographed on silica gel using 15% ethyl acetate in hexane as eluent to yield a white powder (3.9 g, 84%). The product was recrystallized from perfluoromethylcyclohexane on cooling from reflux at 1 °C/h over 2 days to yield colorless crystals. ¹H NMR (500 MHz, C₂D₂Cl₄, 105 °C) δ 0.98 (t, 3H, ³J_{HH} = 6.8 Hz, CH₃), 1.3–1.5 (m, 22H, CH₂), 1.58 (quintet, 2H, ³J_{HH} = 7.1 Hz, OCH₂CH₂CH₂), 1.89 (quintet, 2H, ³J_{HH} = 6.9 Hz, OCH₂CH₂), 4.07 (t, 2H, ³J_{HH} = 6.4 Hz, OCH₂CH₂), 4.52 (t, 2H, ³J_{HF} = 13.1 Hz, OCH₂CF₂), 7.18 (s, 1H, ArH), 7.24 (s, 1H, ArH) ppm; ¹³C NMR (125 MHz, C₂D₂Cl₄, 105 °C) δ 13.50, 22.24, 25.68, 28.92, 28.93, 28.98, 29.17, 29.20, 29.27, 29.28, 31.56, 68.25 (t, ²J_{CF} = 27.1 Hz), 70.88, 111.86, 112.53, 119.32, 121.83, 149.03, 152.67 ppm; ¹⁹F NMR (470 MHz, C₂D₂Cl₄, 105 °C) δ –80.28 (3F, CF₃), –118.08 (2F, CH₂CF₂), –120.24 (8F, CF₂), –120.45 (4F, CF₂), –121.35 (2F, CF₂), –121.82 (2F, CF₂), –124.72 (2F, CF₂CF₃) ppm; FDMS: *m/z* [*u e*^{–1}] 1018.9 (100%), [*M*⁺]; calcd: 1018.0 (C₃₀H₂₉⁷⁹Br⁸¹BrF₃O₂); Anal. calcd for C₃₀H₂₉Br₂F₂₃O₂: C, 35.38; H, 2.87; found: C, 35.43; H, 2.93.

Spreading solutions (1 mg·mL^{–1}) were prepared in hexane (analytical grade). Water was purified to a resistivity of 18.2 MΩ·cm using a Milli-Q filtration system (Millipore).

2.2. Monolayer Isotherms and Monolayer Transfer. Surface pressure versus molecular area (π –*A*) isotherms were recorded on three different Langmuir troughs made of hydrophobic Teflon, equipped with two movable hydrophilic polyoxymethylene barriers: KSV Minitrough 4 for ISR 400 (KSV Instruments Ltd., Finland), appropriately modified Langmuir-Trough RK1 (Riegler and Kirstein GmbH, Potsdam, Germany) and a trough dedicated to scattering experiments.²⁴ The surface pressure, π , was measured using the Wilhelmy plate method. Temperature was regulated to 20.0 °C. An equilibration time of 5 min after spreading was used for solvent evaporation.

The monolayers were compressed up to the desired surface pressure (compression speed 5 mm·min^{–1}) and transferred onto plasma-cleaned (10 min Ar plasma) silicon wafers. The silicon substrates were positioned with a slight inclination in the aqueous subphase before spreading. The monolayer was transferred by removal of the subphase from the trough with a peristaltic pump (Minipuls 3, Abimed, Gilson Inc., United States) with a pump rate of approximately 10 mL·min^{–1}, thereby lowering the monolayer onto the wafer.²⁵

Monolayers without compression for SFM imaging were prepared by direct evaporation (overnight) of one drop (submonolayer coverage) of the amphiphobe solution (*c* = 1 mg·mL^{–1}) spread on an aqueous film on a freshly cleaned wafer.

2.3. SFM Measurements. The transferred films were analyzed with a scanning force microscope (Dimension 3100, Veeco Instruments, United States, and MFP-3D, Asylum Research, United States) in tapping mode, equipped with sharpened, aluminum backside coated silicon

cantilevers (Olympus OMCL-AC240TS, nominal tip radius <7 nm, resonance frequency 50–90 kHz, spring constant 0.7–3.8 N·m^{–1}). The cantilevers were put on a glass coverslip with the tip side facing air and were Ar plasma cleaned (Plasma Cleaner/Sterilizer PDC-002, 200W, Harrick Scientific Corp., United States) for 30 s at a pressure of approximately 1.6 mbar.

For Kelvin probe force microscopy (KPFM) measurements the chip was electrically connected to the chip holder using conductive silver paste (Fluka, for electron microscopy). SFM and KPFM measurements were performed under ambient conditions (room temperature, air). Imaging of F12H12, F12H20, and F11H1-core-H12 samples was performed at the lowest possible tapping forces characterized by the ratio of free amplitude/amplitude set point²⁶ of 0.96 and a peak offset of –3%. The free amplitude was determined to be the amplitude of the cantilever at peak maximum before approaching the surface. Even then we observed in some cases that material was dislocated or removed by the tip during the measurements, in particular in the case of F11H1-core-H12 films. The generated “holes” in the surface micelle layer were used to estimate the layer thickness. The SFM topographic images were flattened and analyzed using Gwyddion Software (www.gwyddion.net).

KPFM is an operation mode, which is sensitive to local variations in the surface potential of materials. Here, the detection of the surface potential is achieved.²⁷ First the topography is scanned, and then the topographic profile is followed by a second scan at a defined distance from the surface. During this scan the mechanical excitation is switched off and an AC bias of 2000 mV is applied to the tip while the sample remains grounded. An additional variable DC potential is applied at the tip in order to nullify the oscillation amplitude of the cantilever by a feedback loop. This specific DC potential value is recorded at each raster point and is taken as the Kelvin potential difference between the tip and the sample surface. The KPFM images were flattened using median line correction.

2.4. Neutron Reflectivity. Neutron reflectivity experiments were performed at the air/water interface using the dedicated Langmuir trough on the AMOR reflectometer at the Swiss Spallation Neutron Source (SINQ) at the Paul Scherrer Institute, Switzerland, with D₂O as subphase. The instruments and the procedure used are described elsewhere.^{28,29} Measurements were made at three incident angles (0.6, 1.4, and 2.4°), which gave a range of momentum transfer *Q* (with $Q = (4\pi \sin \theta)/\lambda$, where θ is the glancing angle of incidence and λ is 3.14 and NOT the surface pressure (same symbol)) from 0.1 to 1.5 nm^{–1}.

All data were analyzed using Parratt32 software, version 1.6 (Helmholtz-Zentrum Berlin für Materialien und Energie GmbH Germany).³⁰

3. RESULTS

3.1. Isotherms. The surface pressure/molecular area isotherms for F12H12, F12H20, and F11H1-core-H12 are shown in Figure 2. All isotherms comprise a first increase in surface pressure that occurs at surface areas *A*₀ of ca. 33–34 Å²·molecule^{–1} for F12H12, at 27–32 Å²·molecule^{–1} for F12H20, and at 35–37 Å²·molecule^{–1} for F11H1-core-H12. *A*₀ is the surface area at zero surface pressure extrapolated from the slope between 2 and 6 mN·m^{–1}. A stable monolayer is formed up to the limiting area (collapse area) *A*_c = 31–33 Å²·molecule^{–1} for F12H12, *A*_c = 25–28 Å²·molecule^{–1} for F12H20, and *A*_c = 33–34 Å²·molecule^{–1} for F11H1-core-H12. The isotherms were completely reversible, without hysteresis, for compression–expansion cycles before the collapse of the monolayer, as we have recently shown.³¹ The measured *A*_c and *A*₀ values for F12H12 are similar to those found in the literature for other semifluorinated alkanes (F8H16 for example in ref 5), which are consistent with the cross section (projection area) of a fluorocarbon chain.

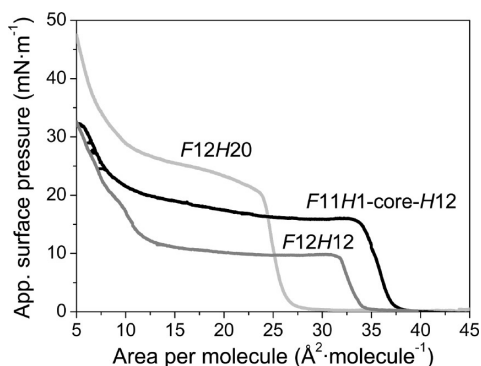


Figure 2. Apparent surface pressure versus molecular area isotherms for *F12H20* (light gray), *F12H12* (dark gray), and *F11H1-core-H12* (black) monolayers at the air/water interface at 20 °C.

After the collapse of the *F12H12* monolayer, the surface pressure remains almost constant at $10 \text{ mN}\cdot\text{m}^{-1}$ down to an area of $13 \text{ \AA}^2\cdot\text{molecule}^{-1}$. The *F12H20* and *F11H1-core-H12* molecules show similar behavior, but with a slight increase in pressure and slope in the “plateau region”. Then, in all cases, a second steep pressure increase occurs at an area of ca. $10 \text{ \AA}^2\cdot\text{molecule}^{-1}$, which is approximately one-third of the monolayer collapse area A_c . A similar behavior was reported recently by Gracia Lux et al.³² for several semifluorinated alkanes with different block lengths (*F8H16*, *F8H18*, *F8H20*, and *F10H16*), which was explained by the buildup of a three-dimensional aggregation system. The authors showed that the two- and three-dimensional systems coexist in the plateau region.

3.2. SFM Measurements. **3.2.1. *F12H12* Monolayer Images.** In order to characterize the two-dimensional (2D) self-assembly structure of the *F12H12* monolayers, SFM measurements were performed (Figure 3). Figure 3A shows the SFM topographic image of a monolayer of *F12H12* transferred to a silicon wafer at a lateral pressure of $2 \text{ mN}\cdot\text{m}^{-1}$. The image depicts an array of surface micelles (circles, spirals, and wormlike structures) as previously reported and rationalized for similar derivatives with asymmetric fluorocarbon and hydrocarbon block lengths.^{5,33} These 2D micelles were observed at all surface pressures investigated (from $1 \text{ mN}\cdot\text{m}^{-1}$ up to the collapse) with an average diameter of 25–35 nm. Their average thickness was determined to be $2.1 \pm 0.1 \text{ nm}$ by surface profile analysis. The higher-resolution image in Figure 3B exhibits features within the surface micelles (see white arrows), which suggests that the surface micelles are composed of individual more-uniform substructures (an assembly and structure model will be discussed further below; see also Figure 11 below). Their diameter of 5–15 nm has been estimated by measuring the distance between the centers of adjacent substructures in the SFM images.

At $2 \text{ mN}\cdot\text{m}^{-1}$, the micelles are partially arranged in quite close-packed hexagonal arrays (see dotted circle in Figure 3C). According to the literature, the micelle size varies slightly for other SFA molecules in the range of $1\text{--}10 \text{ mN}\cdot\text{m}^{-1}$, but the micelles progressively move closer together with increasing surface pressure.⁶ However, for the *F12H12* molecule in this surface pressure regime, the relative compression ($\Delta A/A_0$) is only ca. 7% and the applied surface pressure barely influences the micelle packing and size. This hints at a dense micellar organization which results in solidlike viscoelastic properties resembling the behavior of a 2D jammed colloidal system (e.g., glass-like),^{34,35} as measured by interfacial linear rheology.³¹

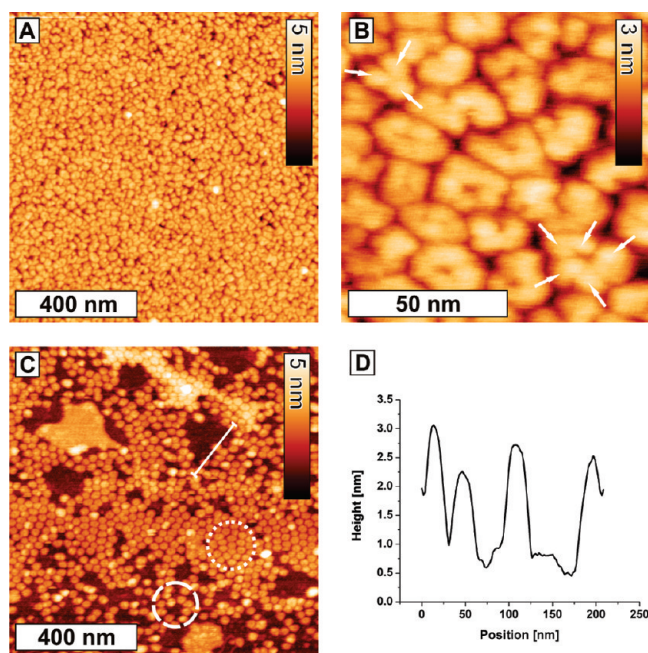


Figure 3. (A) SFM topographic image of an *F12H12* monolayer transferred at $2 \text{ mN}\cdot\text{m}^{-1}$. (B) Zoom-in of the topographic image. Different micelle shapes and individual substructures marked by white arrows are visible. (C) SFM topographic image of an *F12H12* monolayer deposited by direct evaporation of the subphase without compression. The image shows closely packed micelles (dotted circle) as well as disordered regions (dashed circle). (D) Line plot at the location marked in image C. The plot shows the dimensions of one individual surface micelle (height $\sim 2.2 \text{ nm}$, diameter $\sim 23 \text{ nm}$).

A peculiar feature at these surface pressures is the presence of higher three-dimensional (3D) aggregates in the dense layer of surface micelles (Figure 4), which do not show a specific contrast in the surface potential measurements and have not been previously reported in the literature. Up to the collapse, these aggregates are virtually monodisperse (diameter ca. 40 nm; thickness 4.3 nm with respect to the substrate).

In several regions distributed throughout the whole film, the Kelvin probe measurements (image in Figure 4C and Figure S1 in the Supporting Information) reveal domains with lower surface potential, which have only a faint contrast in the topographic (slightly brighter regions with higher layer thickness) and the phase (slightly darker regions) images. These slightly higher domain structures appear denser with less-defined micellar boundaries. The corresponding more negative surface potential difference is independent of the aggregates on top of the micelles, and hints at a different structure/organization of the molecules in these regions (further discussion in section 4.1).

At $10 \text{ mN}\cdot\text{m}^{-1}$, additional larger aggregates appear as flat islands on top of the micelle carpet, which are apparently 3D layered structures associated with the monolayer collapse (Supporting Information, Figure S2). Similar aggregates have been reported for *F8H20* diblocks, at high surface pressures, after the collapse of the monolayer.³²

In order to see if the micelles self-assemble without application of lateral surface pressure by the trough barriers, monolayers were also prepared by simple solution evaporation on a water film on top of a wafer at very low surface coverage and observed by SFM (Figure 3C) after drying. The surface micelles are still

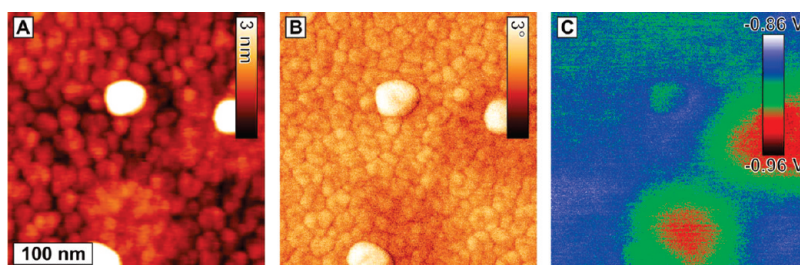


Figure 4. SFM images of an *F12H12* film transferred at $5 \text{ mN} \cdot \text{m}^{-1}$. (A) Topographic image showing the micelle carpet and larger 3D aggregates (average diameter 40 nm; average thickness with respect to the substrate 4.3 nm) and domains of slightly higher layer thickness. (B) Corresponding phase image showing a slight phase contrast (0.5°) for the domains. (C) Corresponding Kelvin potential image of the same region with domains of lower surface potential, while the 3D aggregates do not show a significant surface potential difference.

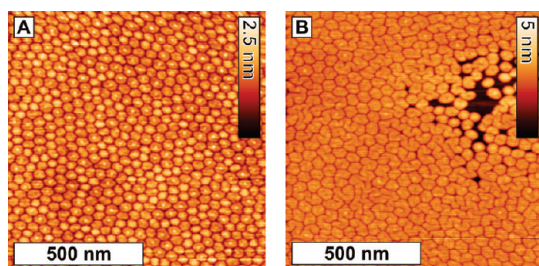


Figure 5. SFM images of an *F12H20* monolayer transferred at $2 \text{ mN} \cdot \text{m}^{-1}$. (A) Topography of a densely packed, partially hexagonally organized monolayer. (B) Topographic image of a different region showing hexagonal as well as more elongated surface micelles.

present, but alternating between dense zones and more disordered ones (as already observed for *F8H16* monolayers).³³ In the dense zones the micelles are already packed in hexagonal arrays even without compression of the layer. Larger and denser domains in the topographic and phase images are also visible in the Kelvin probe microscopy measurements by a lower surface potential (Supporting Information, Figure S3), while the higher 3D aggregates are indiscernible by KPFM. The surface potential difference between individual surface micelles and the surrounding surface area has also been determined as -0.6 V for the edge of a film without compression (see Figure S4 in Supporting Information). This value is consistent with KPFM measurements in the literature.^{36–38}

3.2.2. *F12H20* Monolayer Images. *F12H20* monolayers were also imaged by SFM: the molecules self-assemble in a hexagonal pattern of hexagonally shaped surface micelles, besides extended, wormlike surface micelles, which also form in various regions (Figure 5). Compared to *F12H12*, the micelles are slightly larger (ca. 50 nm diameter), but no fine structure (primary aggregates) is discernible. Each surface micelle appears in very close contact with all neighboring micelles, inducing hexagonal deformation.

A high-resolution SFM image of an *F12H20* film transferred at $2 \text{ mN} \cdot \text{m}^{-1}$, shown in Figure 6, also demonstrates well the coexistence of hexagonal micelles and elongated structures in a more interlocked 2D system, but it does not show any fine structure within the individual micelles. This change in surface morphology from nearly circular to stronger interlocked and more extended micelles explains the shift in the rheological behavior measured by us.³¹ *F12H20* monolayers show a self-similar response typical of gel-like systems, apparently due to the junctions and interlocking of the extended micelles.^{39,40}

The corresponding KPFM image (Figure 6C) does not show any contrast within the dense surface micelle film, and

only the substrate is visible where holes in the monolayer are present.

3.2.3. *F11H1*-core-*H12* Monolayer Images. SFM images obtained for an *F11H1*-core-*H12* monolayer transferred at $2 \text{ mN} \cdot \text{m}^{-1}$ are presented in Figure 7. A different type of surface micelles is observed, consisting of straight ribbons with an approximate length of up to ca. 400 nm (or smaller, depending on the monolayer preparation conditions, Figure 7A,C,D) and an average width of 30–40 nm, similar to the diameter of the circular micelles formed by the *F12H12* molecules. As for *F12H12* and *F12H20*, the micelles appear close-packed even at low surface pressures. Striations of ca. 10 nm width are visible within the ribbons parallel to their longitudinal axis (Figure 7B), again reminiscent of the substructure dimension in the surface micelles of *F12H12*. The micelles themselves exhibit a fan-like structure with micelles spreading and branching from an initial branching point (Figure 14 and Figure S5 in the Supporting Information). Such surface micelles also form a dense layer in the absence of external surface pressure, as in the case of *F12H12* (Figure 7C). A similar surface-micellar structure can be observed on the film obtained without compression, after evaporation, as seen in Figure 7A, which shows a close-packed organization of straight ribbons, but with a less-pronounced dendritic growth. Again, in interfacial rheology experiments the interdigitated micellar organization was found to influence the monolayer viscoelastic properties, which reflect a strongly correlated, self-similar viscoelastic solid-like material.^{31,39,40} KPFM images of the samples do not show any inhomogeneities in the micelle carpet (Figure 7F), but show the potential difference between sample and substrate.

Besides this difference of micellar morphology depending on the preparation conditions, we also found a substantial reorganization of the monolayer structure on the solid support after extended periods of time. An example of the morphology change of an *F11H1*-core-*H12* monolayer on a silicon substrate after 2 months is shown in Figure S6 in the Supporting Information. Such long-term film reorganization is expected to be induced by the difference in interfacial energy between the *F11H1*-core-*H12* monolayer and the silicon substrate, which is different from the water subphase.

3.3. Neutron Reflectivity. Monolayers of *F12H12* equilibrated at seven different surface pressures (from 2 to $10 \text{ mN} \cdot \text{m}^{-1}$) were investigated by neutron reflectivity measurements, as shown in Figure 8 (full set of data in the Supporting Information, Figure S7). In neutron reflectivity measurements, the variation of the reflectivity with the momentum transfer Q depends on the scattering length density profile normal to the interface.

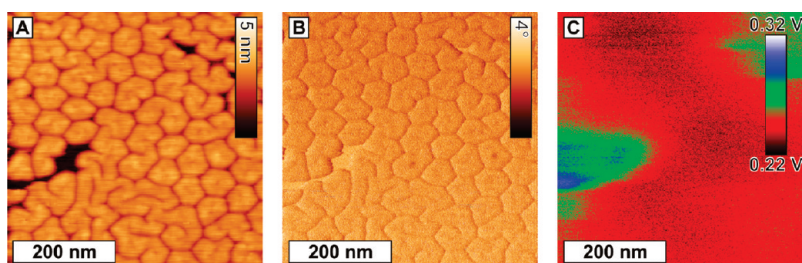


Figure 6. Higher-resolution SFM and KPFM images of an $F12H20$ monolayer transferred at $2 \text{ mN} \cdot \text{m}^{-1}$. (A) Topographic, (B) phase, and (C) Kelvin probe images.

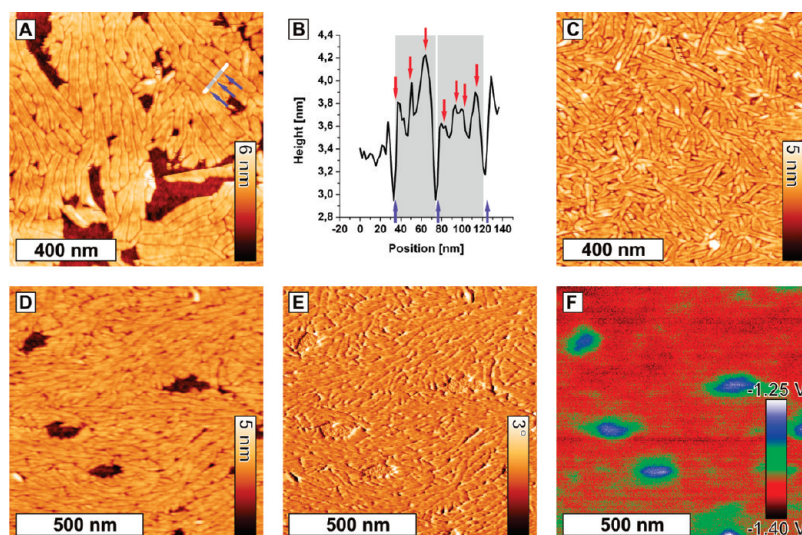


Figure 7. SFM images of $F11H1$ -core- $H12$ films. (A) Topographic image of an $F11H1$ -core- $H12$ film transferred at $2 \text{ mN} \cdot \text{m}^{-1}$. (B) Line plot at the location marked in image A. Blue arrows mark the edges between neighboring micelles, and red arrows mark substructures inside each micelle. (C) Topographic image of an $F11H1$ -core- $H12$ film prepared by direct evaporation of the subphase at a nominal surface pressure of $0 \text{ mN} \cdot \text{m}^{-1}$. (D)–(F) SFM images of an $F11H1$ -core- $H12$ film transferred at $5 \text{ mN} \cdot \text{m}^{-1}$: (D) topographic, (E) phase, and (F) Kelvin potential images.

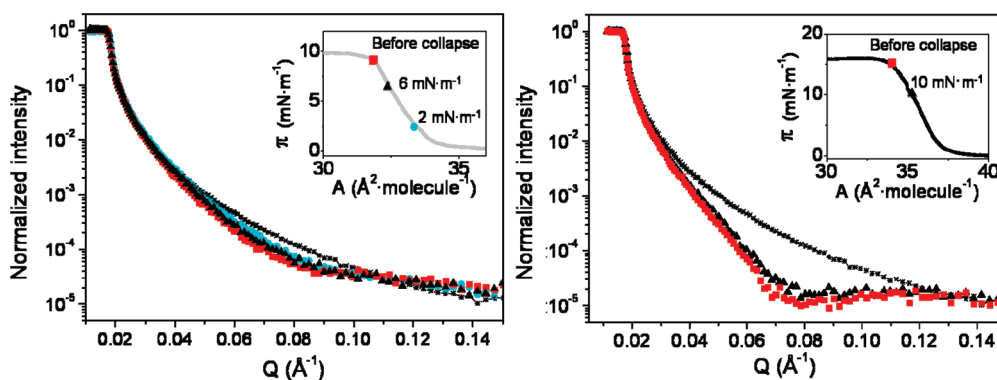


Figure 8. Neutron reflectivity curves on D_2O and corresponding π – A isotherms in the insets. Left: $F12H12$ monolayers at $2 \text{ mN} \cdot \text{m}^{-1}$ (blue circles), at $6 \text{ mN} \cdot \text{m}^{-1}$ (black triangles), and just before collapse (red squares). Right: $F11H1$ -core- $H12$ monolayers at $10 \text{ mN} \cdot \text{m}^{-1}$ (black triangles) and at collapse (red squares). The reflectivity curves for the neat D_2O subphase are indicated by the asterisks (*).

Generally, oscillations (Kiessig fringes) may be visible in neutron reflectivity profiles, depending on the thickness of the layer at the air/water interface and with respect to the position and the difference in scattering contrasts between the respective interfaces. For the particular $F12H12$ monolayers presented here, the intensity of the neutron reflectivity curves decreases steeper with increasing surface pressure, but no specific minimum is observed

(no Kiessig fringes visible), which may lead to difficulties in the interpretation as discussed in section 4. However, neutron reflectivity measurements present the advantage of investigating the monolayer structure directly at the air/water interface without transfer. Thus, even in the absence of characteristic minima, fitting of the curves is attempted, taking into account different possible packing models by variation of the structural parameters

(number of layers, and for each layer, layer thickness, scattering length density, and surface roughness).

These parameters can be estimated from data provided by complementary techniques, such as the molecular area from isotherms and the monolayer heights from SFM images:

- The scattering length density (SLD) of each compound is estimated from ref 41 providing the bulk density of *F12H12* (i.e., $1.6 \text{ g} \cdot \text{cm}^{-3}$ according to Nunez et al.¹⁷).
- The thickness of the monolayer can be calculated from a simple bulk volume model as $d = 25 \text{ \AA}$, using the weight of the deposited material, the bulk density of *F12H12* molecules, and the molecular area in the isotherm at $5 \text{ mN} \cdot \text{m}^{-1}$. Moreover, based on a molecular structure model,¹² a fully stretched molecule with all-trans conformation will have the fully extended length of $d(\text{FnHm}) = 1.3n + 1.265m + 2.58 \text{ \AA}$, which leads to a length of 33.4 \AA for *F12H12*, consistent with the computer model. Those two values (calculated from the isotherm and the fully extended model) provide a reasonable range of possible layer thicknesses. The thickness estimated from the SFM measurements is around 21 \AA . Assuming the error in estimating the height for soft materials is in the range of 20–30%, we obtain a corrected thickness of $25\text{--}27 \text{ \AA}$.
- The molecular roughness of the subphase can be estimated between one and two diameters of a water molecule, so approximately $3\text{--}6 \text{ \AA}$. A fit of the reflectivity curve obtained for the neat D_2O surface indeed provides a value of 5 \AA for the subphase roughness. Then the roughness of the different layers is assumed to be above twice this value (roughness of the subphase + specific roughness of the layer). Consistently, the SFM measurements provide a minimum roughness value of 15 \AA , which is used as a first guess for the fitting parameter.

For *F11H1-core-H12*, the scattering profiles for the two surface pressures are qualitatively similar (Figure 8, right). The reflectivity curves show one reflectivity minimum at ca. $Q = 0.07 \text{ \AA}^{-1}$ and a curve shape (Kiessing fringes) characteristic of a monolayer. The same considerations (based on isotherms and SFM data) are used to estimate the possible range of parameters (scattering length density, roughness, and thickness). For the layer thickness, the bulk estimation from the isotherm data provides an approximate value around $d = 31 \text{ \AA}$. The fully extended length would be 39.4 \AA , assuming an approximate height of the core around 6 \AA (according to a computer-generated molecular structure model). The thickness estimated from the SFM measurements is ca. 22 \AA , which here again must be considered with caution. It is possible that flat-lying molecules cover the substrate in the “empty” zones between the surface micelles, which are used as a reference level for the height measurements. This value is clearly underestimating the extended chain length; thus we assume the possible layer thickness to be in the range of $30\text{--}40 \text{ \AA}$ based on the isotherm data and the fully extended chain model.

For the asymmetric SFA *F12H20*, no neutron reflectivity data were recorded due to the lack of resources (sample unavailability at the time of the measurements).

4. DISCUSSION

4.1. Structural Model for *F12H12*. For semifluorinated alkanes spread at the air/water interface several possible models can be proposed, as presented in Figure 9.

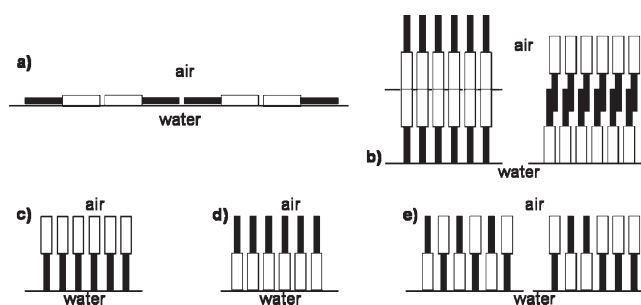


Figure 9. Different models for *F12H12* structure at the air/water interface (side view as cut through the film and the water surface). (a) Horizontal (flat-lying molecules) (b) Vertical multilayer. (c)–(e) Monolayer with vertical orientation: (c) F-block up, (d) H-block up, and (e) head-to-tail orientation (left, antiparallel; right, random). The white rectangles represent the F-blocks and the black ones represent the H-blocks (for chemical structures, refer to Figure 1).

In the dense layer below the collapse surface pressure, the existence of multilayer structures is excluded based on the height data from the SFM measurements and the molecular surface requirement from the isotherms. The area data provide direct information on the film geometry and volume, which is consistent with the deposited material volume in the spreading solution: no material is lost during spreading and compression. The measured surface area of ca. $35 \text{ \AA}^2 \cdot \text{molecule}^{-1}$ corresponds to the projection area of the perfluoroalkyl chain along the molecular main axis. The data suggest a monolayer with a vertical chain orientation with the long molecular axis essentially oriented perpendicular to the water surface. A flat phase (Figure 9a) may also be present, coexisting with a vertical phase as proposed by Semenov et al.³³ However, at the surface pressures investigated, this phase cannot be predominant according to the measured molecular surface area, and would not be detected in neutron reflectivity experiments due to a too low thickness for the given scattering length density. Indeed, the SFM topographic images indicate that the substrate surface, which is visible between the surface micelles, is partially covered with such flat-lying molecules. The surface roughness of the free regions is enhanced compared to a blank silicon wafer. Another hypothetical case of a highly bent molecular structure with both the F- and the H-chains pointing toward the air phase could be envisioned, where the polar $\text{CF}_2\text{--CH}_2\text{--}$ bond would be in contact with the water phase. This model would require a very strong deformation of the molecule with an unfavorable proximity of the F- and H-chains, which is not supported at all by the molecular surface requirement in the isotherms and the layer height in the SFM images. This structure is thus fully excluded from the discussion here.

Considering a monolayer structure with vertically oriented molecules, three different packing models can be proposed (Figure 9c–e). The fluorocarbon chains are a priori expected to orient toward the air (Figure 9c), rather than toward the aqueous phase, because of their larger hydrophobicity and higher affinity for gases compared to hydrocarbon chains, which results in a lower surface energy of the formed F-surface of the monolayer. This configuration has been established for *F8H16* by X-ray reflectivity.⁵ However, molecular dynamics simulations of *F12H18* molecules support the existence of antiparallel molecular packing at short times (Figure 9e),⁴² which was also proposed for *F8H18* films based on X-ray reflectivity data,¹⁰ but this remains a matter of discussion.²

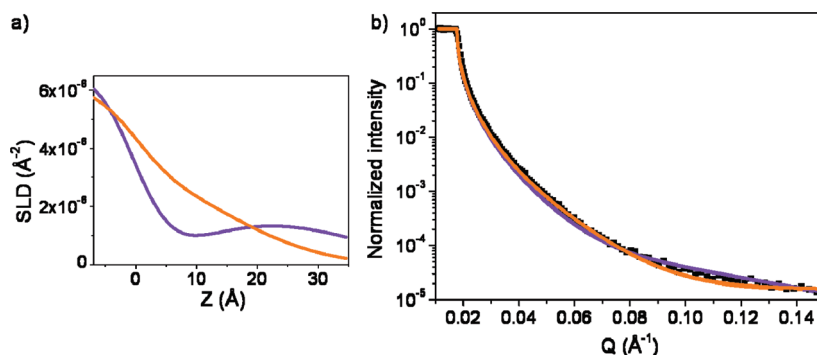


Figure 10. (a) Evolution of the scattering length density (SLD) for “semi-bilayer” models: (violet) F-block toward the air with a thickness of 14 Å and a roughness of 15 Å for both half-layers; (orange) H-block toward the air with a thickness of 14 Å and a roughness of 15 Å for both half-layers. (b) Neutron reflectivity curve (black squares) for *F12H12* at 4 mN·m⁻¹ and fits for both models: (violet) F-block toward the air (background 0.5 × 10⁻⁵); (orange) H-block toward the air (background 1.5 × 10⁻⁵).

The fitting of the neutron reflectivity curves is used as a basis to discriminate the different possible structural models c–e. Due to the shape of the curves (absence of fringes, mentioned in section 3.3), several solutions can exist for the fitting of one curve. However, an important constraint on the selection of model parameters is that they should be physically reasonable based on the data from complementary techniques. Providing the parameters discussed in section 3.3 (thickness of the monolayer estimated between 25 and 33 Å, and roughness ca. 15 Å), three different models c–e in Figure 9 have been tested for the curve simulation.

Hypothetical Model e: Assuming alternating head-to-tail orientation, model e, the best fitting (with the best fit quality and the most reasonable parameters) would be obtained for a hypothetical thickness around 20 Å, with an average scattering length density and a roughness around 15 Å. From an experimental point of view this assumption would require that ca. 20% of the material is lost after spreading, in order to yield the measured molecular surface requirement in the isotherm, which is not supported by experimental observations. Moreover, such a molecular orientation would not lead to a lateral packing strain (and associated layer curvature, see discussion of Figure 11 below) and thus should not induce any surface micelle formation, but rather pack homogeneously in extended domains.

Hypothetical Models c and d: On the contrary, the data can be fitted with a two-layer model (Figure 9c,d) with parameters within the estimated ranges from the experimental results. It appears then that the most accurate model that can be proposed consists of a monolayer with parallel molecules, but as shown in Figure 10, it is not possible to discriminate only with the neutron reflectivity data between model c with F-block up, and model d with H-block up: both models allow reasonably accurate curve simulations.

In order to gain some insight on the molecular orientation of the molecules, KPFM was employed. The KPFM technique is sensitive to the effective dipole moment parallel to the tip–surface axis (i.e., the surface normal) and the permittivity of the material between the tip and the substrate.⁴³ In the semifluorinated alkanes the major contributions to the effective dipole are the molecular fragment dipoles of the CF₃– group and the central –CF₂–CH₂– bond.³⁶ El Abed et al.¹⁰ and Broniatowski et al.⁴⁴ investigated the macroscopic surface potential of *F_nH_m* molecules at the air/water interface. Both attributed a negative surface potential to the fluorinated part of the respective molecules being oriented toward the air. KPFM studies and related

techniques on molecules with *F_nH_m* fragments have been employed by Chi et al.,⁴⁵ Sugimura et al.,³⁷ Alexander et al.,³⁶ and Magonov et al.,⁴⁶ who interpreted differences in surface potential in terms of –CH₂–CF₂– dipole orientation. A surface potential difference at the air/water interface of –0.8 V has been proposed for a vertical molecular orientation with the fluorinated part of the molecules oriented toward the air (or for transferred layers –0.6 to –0.7 V relative to a Si wafer surface).^{36,38} Changes in the surface potential properties can have several possible explanations. The presence of included water would lead to slight changes in topographic, viscoelastic, and electric properties. A difference in the micellar density or a change in their orientation would also induce modifications of the surface potential, as all three molecules *F12H12*, *F12H20*, and *F11H1-core-H12* exhibit a strong dipole moment.

As observed in section 3.2.1, the majority of the *F12H12* monolayer area does not show any local potential inhomogeneities in the Kelvin probe measurements on the micelle carpet: in these regions the molecule distribution must be homogeneous at least at the length scale of the KPFM lateral resolution (ca. 30 nm).²⁷ A surface potential difference of about –0.6 V with respect to the silicon substrate was measured for individual micelles (see Supporting Information, Figure S4), in agreement with Kelvin potential variations of *F12H8* and *F14H20* molecules measured on a Si-wafer substrate.^{36–38} As a consequence, we conclude that the *F12H12* molecules inside the micelle carpet are oriented vertically with their fluorocarbon part facing air. This would be in good agreement with the literature data:² the molecular orientation is similar to the one established by X-ray reflectivity measurements for *F8H16* monolayers,⁵ which present the same lateral organization with hexagonal arrays of disklike surface micelles. Several domains with a more negative surface potential with respect to the micelle carpet could also be observed in some regions (see Figure 4C). It appears that the surface micelles are packed more densely in these domains, which is also supported by the slightly increased height in the topographic images and the reduced intramicellar contrast. Such a denser packing could induce a more vertical orientation of the molecular axis and thus of the associated molecular dipole –CF₂–CH₂–, which would result in a more negative surface potential. A second possibility is the existence of domains consisting of molecules with a different orientation (molecules upside down or in an alternating packing), but this orientation is expected to lead to a smaller surface potential difference. The

most probable scenario is a denser packing of the monolayer, but at the current state we cannot distinguish between these possibilities with the SFM and KPFM data.

The parallel orientation is apparently driven by phase separation between the F- and H-blocks. Considering this molecular orientation, a simple model for the surface micelle formation can be proposed as a hypothesis (Figure 11). The buildup of isotropic packing strain due to the volume mismatch between the thick F-block and the thin H-block leads to the formation of “muffin” shaped structures (Figure 11A): the molecules aggregate into a curved monolayer which is counteracted by the planar water surface. The increasing packing strain between the layer curvature and the planarizing water surface tension, as well as electrostatic interactions (unfavorable orientation of the dipoles), limit the size of the primary aggregates. These primary aggregates, corresponding to the substructures observed in SFM, assemble to bigger clusters containing on average five units (spirals, circular, or elongated surface micelles, also discussed in the literature) due to attractive capillary forces.^{47–49} As the primary aggregates have inclined walls (due to the packing strain/layer curvature), optimal contact between aggregates is

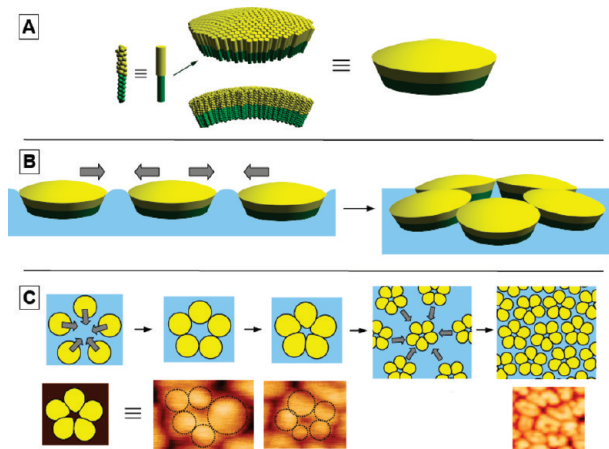


Figure 11. Model proposed for the hierarchical formation of the surface micelles. (A) Self-assembly of the amphiphobic $F12H12$ molecules in parallel orientation with the F-block pointing up to the air into curved primary aggregates with ca. 10 nm diameter. (B) Secondary assembly (side view) of the primary aggregates into clusters of the surface micelles driven by capillary forces. (C) Surface micelle aggregation (top view) with slight deformation of the primary aggregates and comparison to the SFM image details.

enabled by aggregate tilting toward neighboring aggregates and the cluster center. This tilting will minimize contact with surrounding aggregates outside the cluster and explains the appearance of the surface micelles instead of a simple extended hexagonal packing of the primary aggregates (Figure 11B). Slight deformation in the contact regions between the primary aggregates can occur, due to the mobility of the $F12H12$ molecule and the flexibility of the aggregates.

This model is in accordance with other molecular assembly models proposed in the literature.^{5,6,33} Both the micelles and their arrangements are stabilized by a balance of factors that minimize the system free energy: electrostatic interactions due to dipole moments of fluorocarbons, interfacial tension, and hydrophobic interactions.³³

The orientation and packing structure of $F12H20$ molecules is considered to be similar to that of $F12H12$, based on the literature data, the analogous behavior in isotherms, and the similar micellar organization imaged by SFM.

4.2. Structural Model for $F11H1$ -core- $H12$. Considerations similar to those for the $F12H12$ molecules can be proposed for the packing models of $F11H1$ -core- $H12$, consisting of monolayers with vertical orientation of the F-block or H-block pointing upward, or with antiparallel molecular orientation (alternating or random). Here again neutron reflectivity measurements were used to discriminate the different molecular orientations. A procedure similar to that previously reported for $F12H12$ can be applied for the core-extended molecule $F11H1$ -core- $H12$. The parameters, possible thickness and roughness, are discussed in section 3.3.

The different possible models were used to fit the neutron reflectivity curves. For the hypothetical “head-to-tail” configuration, two models can be anticipated with either isotropic scattering length density (model A in Figure 12) or a well-defined aromatic core position as intermediate layer (model B in Figure 12).

Figure 13 depicts the best fitting that can be obtained for each model. It appears that only a structural model consisting of molecules with mixed/alternating orientation can be used. Both mixed-orientation models A and B (from Figure 12) lead to an accurate simulation, providing layer thicknesses of 40 and 38 Å, respectively. As shown in the inset in Figure 13b, it is not possible to further discriminate these two models due to the poor measurement statistics obtained at high momentum transfer (Q).

From the fitting results the molecular orientation appears to be different from that of the $F12H12$ molecule as a consequence of the central aromatic core (PhBr_2).

A second noticeable difference between the two types of amphiphobes is the surface micelle shape as observed in section

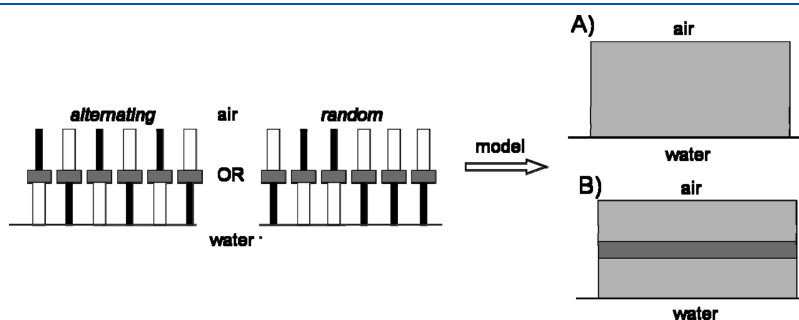


Figure 12. Models for antiparallel orientation (left: alternating and random chain packing; for chemical structures, refer to Figure 1). Model A: globally averaged scattering length density. Model B: triple layer with the upper and lower parts having the same average scattering length density (identical to an averaged $F12H12$) and the center region corresponding to a well-defined aromatic core layer.

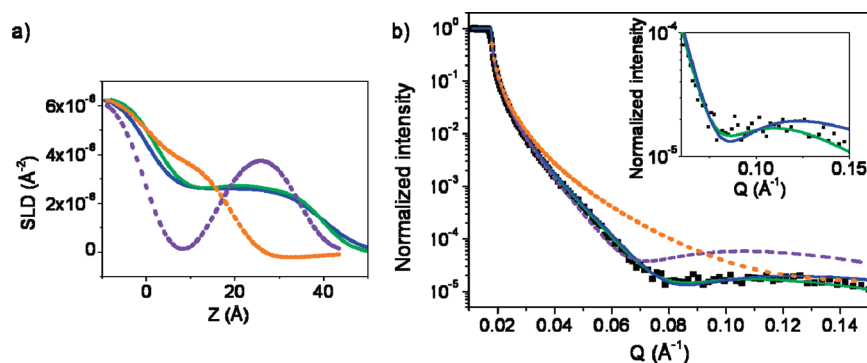


Figure 13. (a) Evolution of the scattering length density (SLD) for different models. Antiparallel packing: model A (green line), thickness of 40 Å and roughness of 7 Å; model B (blue line), thickness of 16.5 Å and roughness of 5 Å for both the upper and lower alkyl chain regions (F- and H-blocks mixed), thickness of 5 Å and roughness of 5 Å for the core layer. Parallel packing: three-layer model with F-block up (violet dashed line), thickness of 15 Å and roughness of 5 Å for both H-block and F-block layers and thickness of 5 Å and roughness of 5 Å for the core layer; three-layer model with H-block up (orange dashed line), thickness of 15 Å and roughness of 10 Å for both H-block and F-block layers and thickness of 5 Å and roughness of 5 Å for the core layer. (b) Neutron reflectivity curve at $10 \text{ mN} \cdot \text{m}^{-1}$ for F11H1-core-H12 (black squares) and fits for the different models proposed: (green line) antiparallel model A (background 8×10^{-6}), random model (blue line) B (background 1×10^{-5}), and F-block up and down without background (violet and orange dashed lines as in (a)).

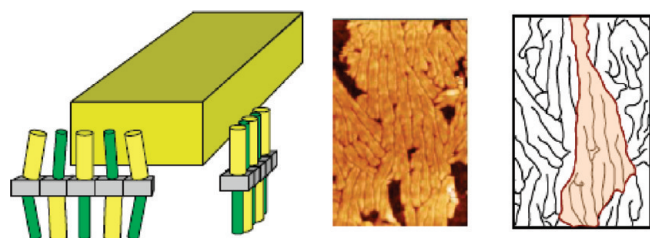


Figure 14. Left: Model proposed for the hierarchical packing structure of the F11H1-core-H12 molecules into a ribbon element (yellow-green block). Center: SFM image with observed dendritic ribbon structure. Right: Line illustration of a single dendritic domain with a fingering of the ribbons.

3.2. The F11H1-core-H12 self-assembles into ribbons with a length about 10 times larger than the average diameter of the circular micelles observed for F12H12 monolayers. The aromatic core induces a structural as well as a dipole asymmetry in the molecule, compared to the rotational symmetry of the F12H12 along the molecular main axis, which induces a strong packing anisotropy. While the antiparallel orientation of the molecules is suggested by the fitting of the neutron reflectivity data, such packing should not lead to a strain buildup by volumetric mismatch if only the F- and H-blocks would be considered. Extended monolayer domains would be expected for this molecule type, ignoring the anisotropic core structure. Since well-defined surface micelles exist, obviously, a different mechanism limiting the layer extension due to the presence of the aromatic core in the layer must be present, which along the direction of the phenyl face or the phenyl edge leads to a packing structure with elongated micelles. The packing structure model in Figure 14 may be proposed as a hypothesis. The aromatic core has about the same thickness as the alkyl chain, so no distortion, but rather a stabilization of the alkyl packing, is expected along the stacking direction of the cores, which is expected to be the long axis of the elongated surface micelle. On the other hand, the core is much wider than the cross section of the alkyl chain; thus along the direction of edge-on stacking a strong packing mismatch is

expected to limit the width of the surface micelle along the short axis.

5. CONCLUSION

The original 2D structure of non-classical amphiphobic molecules with symmetric F- and H-block lengths was studied by combination of neutron reflectivity and scanning force microscopy, coupled with Kelvin probe force microscopy measurements. As reported in the literature for asymmetric block lengths and shown here for F12H20, both molecules with symmetric chain length (F12H12 and its core extended analogue F11H1-core-H12) form surface micelles when spread at the air/water interface. The symmetry does not appear to play a crucial role as the F12H12 molecules were found to behave like other asymmetric derivatives, e.g., F12H20. With the molecular main axis perpendicular to the air/water interface and the F-block pointing toward the air, they self-organize into 30 nm disk-like surface micelles (or spirals slightly extended), composed of circular 10 nm substructures size-controlled by free-energy minimization. Analogous micellar organization was found for F12H20 molecules, but with a more close packed self-assembly, which induces the coexistence of hexagonally deformed micelles with interlocked extended ones. Conversely, the phenyl ring insertion induces dramatic structural changes with respect to the probable molecule orientation and the resulting micelle shape, consisting of branched elongated structures, but which again feature a 10 nm striation substructure (which appears to be a more general structure motif). These results further illustrate how chemical modifications can be used to tailor the hierarchical self-assembly of such semifluorinated alkanes and to extend their possible applications for driving supramolecular assembly. The changes in micellar organization, i.e., the micelle shape, but also their close packing, are strongly reflected in the viscoelastic properties of the monolayer.³¹ A rigorous structural characterization complemented with interfacial rheological measurements is suggested as a powerful methodology to yield detailed insight into the monolayer characteristics for the rational design of novel molecular architectures in order to target the desired film properties.

ASSOCIATED CONTENT

S Supporting Information. Additional SFM images of F12H12 and F11H1-core-H12 films; neutron reflectivity curves for F12H12 monolayers at the air/water interface. This material is available free of charge via the Internet at <http://pubs.acs.org>.

AUTHOR INFORMATION

Corresponding Author

*E-mail: ujonas@iesl.forth.gr.

ACKNOWLEDGMENT

The authors thank the EU for financial support via the projects ITN COMPLOIDS (Grant FP7-PEOPLE-ITN-2008-234810) and Nanodirect (Grant CP-FP 213948). We thank J. Ochsmann for assistance with X-ray experiments, S. Weber and M. Retschke for assistance with KPFM measurements and valuable discussions, and B. Loppinet for many fruitful discussions.

REFERENCES

- Gaines, G. L. *Langmuir* **1991**, *7* (12), 3054–3056.
- Krafft, M. P.; Riess, J. G. *Chem. Rev.* **2009**, *109* (5), 1714–1792.
- Riess, J. G. *Curr. Opin. Colloid Interface Sci.* **2009**, *14*, 294–304.
- Broniatowski, M.; Dynarowicz-Latka, P. *Adv. Colloid Interface Sci.* **2008**, *138*, 63–83.
- Maaloum, M.; Muller, P.; Krafft, M. P. *Angew. Chem., Int. Ed.* **2002**, *41* (22), 4331–4334.
- Zhang, G. F.; Marie, P.; Maaloum, M.; Muller, P.; Benoit, N.; Krafft, M. P. *J. Am. Chem. Soc.* **2005**, *127* (29), 10412–10419.
- Jacquemain, D.; Grayer Wolf, S.; Leveiller, F.; Lahav, M.; Leiserowitz, L.; Deutsch, M.; Kjaer, K.; Als-Nielsen, J. *J. Am. Chem. Soc.* **1990**, *112* (21), 7724–7736.
- Grayer Wolf, S.; Deutsch, M.; Landau, E. M.; Lahav, M.; Leiserowitz, L.; Kjaer, K.; Als-Nielsen, J. *Science* **1988**, *242*, 1286–1290.
- Zhang, G. F.; Maaloum, M.; Muller, P.; Benoit, N.; Krafft, M. P. *Phys. Chem. Chem. Phys.* **2004**, *6*, 1566–1569.
- El Abed, A.; Fauré, M. C.; Pouzet, E.; Abillon, O. *Phys. Rev. E* **2002**, *65*, 051603.
- Broniatowski, M.; Sandez Macho, I.; Minones, J., Jr.; Dynarowicz-Latka, P. *J. Phys. Chem. B* **2004**, *108*, 13403–13411.
- Lo Nostro, P. *Curr. Opin. Colloid Interface Sci.* **2003**, *8*, 223–226.
- Hoepken, J.; Pugh, C.; Richtering, W.; Moeller, M. *Makromol. Chem.* **1988**, *189*, 911–925.
- Rabolt, J. F.; Russell, T. P.; Twieg, R. J. *Macromolecules* **1984**, *17* (12), 2786–2794.
- Russell, T. P.; Rabolt, J. F.; Twieg, R. J.; Siemens, R. L.; Farmer, B. L. *Macromolecules* **1986**, *19*, 1135–1143.
- Hoepken, J.; Moeller, M. *Macromolecules* **1992**, *25*, 2482–2489.
- Nunez, E.; Clark, C. G.; Cheng, W.; Best, A.; Floudas, G.; Semenov, A. N.; Fytas, G.; Muellen, K. *J. Phys. Chem. B* **2008**, *112* (21), 6542–6549.
- Lee, Y. J.; Clark, C. G., Jr.; Graf, R.; Wagner, M.; Muellen, K.; Wolfgang Spiess, H. W. *J. Phys. Chem. B* **2009**, *113*, 1360–1366.
- Clark, C. G., Jr.; Floudas, G. A.; Lee, Y. J.; Graf, R.; Spiess, H. W.; Muellen, K. *J. Am. Chem. Soc.* **2009**, *131*, 8537–8547.
- Ruiz, J. P.; Dharia, J. R.; Reynolds, J. R.; Buckley, L. J. *Macromolecules* **1992**, *25*, 849–860.
- Nenov, S.; Clark, C. G., Jr.; Klapper, M.; Muellen, K. *Macromol. Chem. Phys.* **2007**, *208*, 1362–1369.
- Baskar, C.; Lai, Y. H.; Valiyaveetil, S. *Macromolecules* **2001**, *34*, 6255–6260.
- Kandre, R. M.; Kutzner, F.; Schlaad, H.; Schlüter, A. D. *Makromol. Chem. Phys.* **2005**, *206*, 1610–1618.
- Als-Nielsen, J. In *Handbook on Synchrotron Radiation*; Brown, G., Moncton, D. E., Eds.; North Holland: Amsterdam, 1991; Vol. 3, pp 471–504.
- Vogel, N.; de Viguier, L.; Jonas, U.; Landfester, K.; Weiss, C. K. *Adv. Funct. Mater.* **2011**, DOI: 10.1002/adfm.201100414.
- Magonov, S. N. In *Encyclopaedia of Analytical Chemistry*; Meyers, R. A., Ed.; John Wiley & Sons Ltd: Chichester, U.K., 2000; pp 7432–7491.
- Berger, R.; Butt, H. J.; Retschke, M. B.; Weber, S. A. L. *Macromol. Rapid Commun.* **2009**, *30*, 1167–1178.
- Gupta, M.; Gutberlet, T.; Stahn, J.; Keller, P.; Clemens, D. *Pramana* **2004**, *63* (1), 57–63.
- Clemens, D.; Gross, P.; Keller, P.; Schlumpf, N.; Koennecke, M. *Physica B* **2000**, *140*, 276–278.
- Braun, C. *Parratt32 Fitting Routine for Reflectivity Data*; HMI: Berlin, 1997–1999.
- Klein, C. O.; de Viguier, L.; Christopoulou, C.; Jonas, U.; Clark, C. J.; Muellen, K.; Vlassopoulos, D. *Soft Matter* **2011**, in press; DOI:10.1039/C1SM05357D.
- Gracia Lux, C. de; Gallani, J. L.; Waton, G.; Krafft, M. P. *Chem.—Eur. J.* **2010**, *16*, 7186–7198.
- Semenov, A. N.; Gonzalez-Perez, A.; Krafft, M. P.; Legrand, J. F. *Langmuir* **2006**, *22* (21), 8703–8717.
- Ozon, F.; Petekidis, G.; Vlassopoulos, D. *Ind. Eng. Chem. Res.* **2006**, *45* (21), 6946–6952.
- Di Cola, E.; Moussaid, A.; Sztucki, M.; Narayanan, T.; Zaccarelli, E. *J. Chem. Phys.* **2009**, *131* (14), 144903.
- Alexander, J.; Magonov, S.; Moeller, M. *J. Vac. Sci. Technol., B* **2009**, *27*, 903–911.
- Sugimura, H.; Hayashi, K.; Saito, N.; Nakagiri, N.; Takai, O. *Appl. Surf. Sci.* **2002**, *188*, 403–410.
- Magonov, S.; Alexander, J. *Beilstein J. Nanotechnol.* **2011**, *2*, 15–27.
- Romeo, G.; Filippone, G.; Fernández-Nieves, A.; Russo, P.; Acerno, D. *Rheol. Acta* **2008**, *47* (9), 989–997.
- Shah, S. A.; Chen, Y.-L.; Schweizer, K. S.; Zukoski, C. F. *J. Chem. Phys.* **2003**, *119* (16), 8747–8760.
- National Institute of Standards and Technology Center for Neutron Research. Scattering Length Density Calculator; <http://www.ncnr.nist.gov/resources/sldcalc.html> (accessed September–December 2010).
- Kim, N.; Shin, S. *J. Chem. Phys.* **1999**, *110*, 10239–10242.
- Taylor, D. M.; Bayes, G. F. *Phys. Rev. E* **1994**, *49* (2), 1439–1449.
- Broniatowski, M.; Minones, J.; Dynarowicz-Latka, P. *J. Colloid Interface Sci.* **2004**, *279*, 552–558.
- Chi, L. F.; Jacobi, S.; Fuchs, H. *Thin Solid Films* **1996**, *284*–285, 403–407.
- Magonov, S.; Alexander, J.; Jeong, S.-H.; Kotov, N. J. *Nanosci. Nanotechnol.* **2010**, *10* (11), 7060.
- Kralchevsky, P. A.; Nagayama, K. *Langmuir* **1994**, *10* (1), 23.
- Kralchevsky, P. A. *Adv. Colloid Interface Sci.* **2000**, *85*, 145–192.
- Kralchevsky, P. A. *Curr. Opin. Colloid Interface Sci.* **2001**, *6* (4), 383–401.